Fe$_2$O$_3$/3DOM BiVO$_4$: High-performance photocatalysts for the visible light-driven degradation of 4-nitrophenol

Kunfeng Zhang, Dr. Yuxi Liu*, Dr. Jiguang Deng*, Shaohua Xie, Hongxia Lin, Xingtian Zhao, Jun Yang, Zhuo Han, Hongxing Dai (Prof.)*

Beijing Key Laboratory for Green Catalysis and Separation, Key Laboratory of Beijing on Regional Air Pollution Control, Key Laboratory of Advanced Functional Materials, Education Ministry of China, and Laboratory of Catalysis Chemistry and Nanoscience, College of Environmental and Energy Engineering, Beijing University of Technology, Beijing 100124, PR China

ARTICLE INFO

ABSTRACT

The three-dimensionally ordered macroporous (3DOM) BiVO$_4$ and its supported iron oxide (xFe$_2$O$_3$/3DOM BiVO$_4$, x = 0.18, 0.97, and 3.40 wt%) photocatalysts were prepared using the ascorbic acid-assisted polymethyl methacrylate-templating and incipient wetness impregnation methods, respectively. Physicochemical properties of the materials were characterized by means of numerous analytical techniques, and their photocatalytic activities were evaluated for the degradation of 4-nitrophenol under visible light illumination. It is found that the BiVO$_4$ possessed a high-quality 3DOM architecture with a monoclinic crystal phase, and the Fe$_2$O$_3$ was highly dispersed on the surface of 3DOM BiVO$_4$. The xFe$_2$O$_3$/3DOM BiVO$_4$ samples much outperformed the 3DOM BiVO$_4$ sample, and 0.97Fe$_2$O$_3$/3DOM BiVO$_4$ showed the best photocatalytic performance (98% 4-nitrophenol was degraded in the presence of 0.6 mL H$_2$O$_2$ within 30 min of visible light illumination) and excellent photocatalytic stability. The introduction of H$_2$O$_2$ to the reaction system could promote the photodegradation of 4-nitrophenol by providing the active •OH species generated via the reaction of photoinduced electrons and H$_2$O$_2$. The pseudo-first-order reaction rate constants (0.0876–0.1295 min^{-1}) obtained over xFe$_2$O$_3$/3DOM BiVO$_4$ were much higher than those (0.0033–0.0395 min^{-1}) obtained over 3DOM or Bulk BiVO$_4$ and Fe$_2$O$_3$/Bulk BiVO$_4$, with the 0.97Fe$_2$O$_3$/3DOM BiVO$_4$ sample exhibiting the highest rate constant. The enhanced photocatalytic performance of 0.97Fe$_2$O$_3$/3DOM BiVO$_4$ was associated with its unique porous architecture, high surface area, Fe$_2$O$_3$ – BiVO$_4$ heterojunction, good light-harvesting ability, high adsorbed oxygen species concentration, and excellent separation efficiency of photogenerated electrons and holes as well as the photo-Fenton degradation process.

1. Introduction

4-nitrophenol (4-NP) is an intermediate of fine chemicals widely used in pesticides, medicines, and dyes. Excessive utilization of 4-NP causes water pollutions that are serious threats to the ecological environment and human health [1]. The 4-NP has been considered as a typical organic contaminant in wastewater [2–4]. Due to the good chemical stability of 4-NP under natural conditions, many methods (e.g., physical adsorption, physical absorption, microbial treatment, and chemical oxidation [5]) have been adopted to remove this toxic compound from wastewater. Although some achievements have been made using these traditional technologies, there are still a lot of unignorable problems, such as high-energy consumption, secondary contamination, and low efficiency. Photocatalytic oxidation is a potential effective technology since it can convert pollutants into harmless products under sunlight irradiation, in which the key issue is the availability of high-efficiency photocatalytic materials.

Although TiO$_2$ is the most commonly used photocatalyst for 4-NP degradation, the wide bandgap energy of TiO$_2$ limits its applications [6–9]. BiVO$_4$ is a kind of n-type semiconductor responsive to visible light, and has been utilized in water splitting, CO$_2$ reduction, and organic pollutants oxidation. Monoclinic scheelite-type BiVO$_4$ attracts much attention due to its nontoxicity, stability, recyclability, and narrow bandgap energy [10]. The photocatalytic performance of BiVO$_4$ is strongly dependent upon its morphology, surface area, crystallite size, bandgap energy, and exposed crystal face [11–14]. Since Kudo and coworkers reported that BiVO$_4$ was an efficient catalyst for water splitting under visible light irradia-

* Corresponding authors.
E-mail addresses: yxliu@bjut.edu.cn (Y. Liu), jgdeng@bjut.edu.cn (J. Deng), hxdai@bjut.edu.cn (H. Dai).

tion [15], many researchers have successfully prepared a number of $BiVO_4$ materials with different morphologies and porous structures for photocatalytic applications. For example, Obregón et al. [16] reported that the needle-like morphological $BiVO_4$ showed a high photocatalytic activity for the degradation of methylene blue (MB). Yu et al. [12] prepared the ordered mesoporous $BiVO_4$ with a high surface area of 59 m^2/g, and observed that this porous $BiVO_4$ exhibited excellent performance for the photodegradation of MB. However, the rapid recombination of photoinduced electrons and holes can lead to relatively low photocatalytic efficiency. In order to improve the photocatalytic activity of $BiVO_4$, deposition of precious metals or transition-metal oxides is an effective pathway. For instance, the $Au/BiVO_4$ [17], $Pd/BiVO_4$ [18], $Cu_2O/BiVO_4$ [19], $AgO/BiVO_4$ [20], and $Co_3O_4/BiVO_4$ [21] composite catalysts showed much better photocatalytic performance than the $BiVO_4$ support.

Iron oxide (Fe_2O_3) is a cheap *n*-type semiconductor with a narrow bandgap energy. However, the easy recombination and slow migration of photogenerated charge carriers and poor conductivity of Fe_2O_3 greatly limit its phocatalytic applications [22]. Therefore, Fe_2O_3 is often coupled with another semiconductor material to form a heterostructure. Furthermore, Fe_2O_3 could act as the Fenton-like catalyst to induce the reaction. The synergistic effect of photo-Fenton and photodegradation processes probably gave rise to better photocatalytic performance of the $BiVO_4$-supported Fe_2O_3 catalysts. Fe_2O_3/TiO_2 with an optimal mass ratio showed better photocatalytic performance than either Fe_2O_3 or TiO_2 due to formation of heterojunction structure that could accelerate the separation of electrons and holes [23]. Shi et al. [22] fabricated the α-Fe_2O_3/CdS nanorod composites, and found that the over-growth of CdS nanoparticles on the α-Fe_2O_3 nanorods increased the surface area, light absorption ability, and charge separation at the interface between α-Fe_2O_3 and CdS, thus improving the photocatalytic degradation of MB. To the best of our knowledge, there have been no reports on the preparation of $BiVO_4$-supported Fe_2O_3 nanomaterials and their photocatalytic degradation of 4-NP under visible light illumination.

Recently, the development of three-dimensionally ordered macroporous (3DOM) materials has been one of hot topics. For example, Srinivasan et al. [24] adopted polystyrene microspheres as template to prepare 3DOM TiO_2 for the degradation of MB. Liu et al. [25] synthesized the 3DOM $BiVO_4$ using the polymethyl methacrylate (PMMA)-templating method, and investigated the degradation of phenol. Furthermore, 3DOM $InVO_4$ [26], 3DOM Bi_2WO_6 [27], 3DOM C_3N_4 [28], 3DOM WO_3 [29], and 3DOM $SrTiO_3$ [30] were also fabricated, in which a slow photon effect of the 3DOM materials (e.g., 3DOM WO_3 [29] and 3DOM $SrTiO_3$ [30]) could exist in photocatalysis. These semiconductor materials exhibited good photocatalytic performance due to their strong light-harvesting capacity and electron transfer ability.

Previously, our group adopted the PMMA-templating method to successfully generate several kinds of 3DOM semiconductor materials, such as 3DOM Co_3O_4 [31], 3DOM Mn_2O_3 [32], 3DOM Al_2O_3 [33], and 3DOM Fe_2O_3 [34]. We observed that the 3DOM-structured nanomaterials showed excellent catalytic performance as compared to their nonporous counterparts. Herein, we report the preparation, characterization, and photocatalytic activities of 3DOM $BiVO_4$ and $x$$Fe_2O_3$/3DOM $BiVO_4$ (x = 0.18, 0.97, and 3.40 wt%) photocatalysts for the degradation of 4-NP.

2. Experimental

2.1. 3DOM $BiVO_4$ fabrication

The PMMA microspheres were synthesized according to the procedure described elsewhere [33], and the average size of PMMA spheres were ca. 300 nm. 3DOM $BiVO_4$ was fabricated using the ascorbic acid-assisted PMMA-templating method [25]. In a typical fabrication, 10.00 mmol of $Bi(NO_3)_3 \cdot 5H_2O$ was dissolved in 9.00 mL of ethylene glycol (EG) and methanol (MeOH) with an EG/MeOH volumetric ratio of 1: 2 at room temperature (RT), obtaining a transparent mixed solution *A* after 1 h of stirring. Then, 10.00 mmol of NH_4VO_3, 10.00 mmol of ascorbic acid was dissolved in 7.00 mL of deionized water and HNO_3 (68 wt%) (H_2O/HNO_3 volumetric ratio = 6: 1) at 70 °C, obtaining a dark green mixed aqueous solution *B*. After solution *A* was added to solution *B* under stirring for 1 h, 2.00 g of the PMMA template was soaked in the above mixed solution for 3 h. After being filtered, the as-obtained wet PMMA template was dried at RT for 12 h. The calcination procedures of the samples are as follows: (i) The dried PMMA template was first calcined in a muffle furnace at a ramp of 1 °C/min from RT to 300 °C and kept at 300 °C for 2 h, then continuously heated at a ramp of 1 °C/min from 300 to 450 °C and maintained at this temperature for 4 h, thus generating the 3DOM $BiVO_4$ support.

2.2. Fe_2O_3/3DOM $BiVO_4$ preparation

The x wt% Fe_2O_3/3DOM $BiVO_4$ (denoted as $x$$Fe_2O_3$/3DOM $BiVO_4$) photocatalysts were prepared via the incipient wetness impregnation route. In a typical preparation, 0.50 g of 3DOM $BiVO_4$ was impregnated with the desired amount of ferric nitrate aqueous solution for 10 min. After that, the mixture was dried at 80 °C for 12 h, and then calcined in a muffle furnace at a ramp of 1 °C/ min from RT to 350 °C and kept at this temperature for 4 h. The results of inductively coupled plasma atomic emission spectroscopic (ICP–AES) investigations reveal that the real Fe_2O_3 loading (x) in $x$$Fe_2O_3$/3DOM $BiVO_4$ was 0.18, 0.97, and 3.40 wt%, respectively. For comparison purposes, we also prepared the non-porous $BiVO_4$ (denoted as Bulk $BiVO_4$) and 0.92 wt% Fe_2O_3/Bulk $BiVO_4$ (denoted as 0.92Fe_2O_3/Bulk $BiVO_4$) photocatalysts using the hydrothermal [25] and incipient wetness impregnation methods, respectively.

All of the chemicals (A.R. in purity) were purchased from Beijing Chemical Reagents Company and used without further purification.

2.3. Photocatalyst characterization

Physicochemical properties of the 3DOM $BiVO_4$ and $x$$Fe_2O_3$/3DOM $BiVO_4$ samples were characterized by X-ray powder diffraction (XRD), Laser Raman, scanning electron microscopy (SEM), transmission electron microscopy (TEM), N_2 adsorption–desorption (BET), X-ray photoelectron spectroscopy (XPS), UV–visible diffuse reflectance spectroscopy (UV–vis DRS), photoluminescence spectroscopy (PL), and ICP–AES. The detailed characterization procedures are described in the Supplementary material.

2.4. Photocatalytic activity evaluation

Photocatalytic activities of the as-obtained samples were evaluated in a quartz reactor (QO250, Beijing Changtuo Sci. & Tech. Co. Ltd.) for the degradation of 4-NP under visible light illumination. The photocatalytic reaction system is shown in Fig. S1 of the Supplementary material. A 300-W Xe lamp was used as the light source, and an optical cut-off filter was used to only permit illumination at $\lambda \geq 400$ nm. The photocatalytic process was conducted at RT as follows: 40.0 mg of the photocatalyst and 0.6 mL of H_2O_2 aqueous solution (30 wt%) were added to 100 mL of 4-NP aqueous solution (initial 4-NP concentration C_0 = 0.4 mmol/L). Before illumination, the mixed solution was ultrasonically treated for 30 min and then stirred in the dark for 2 h to allow the system to establish the adsorption-desorption equilibrium. The temperature
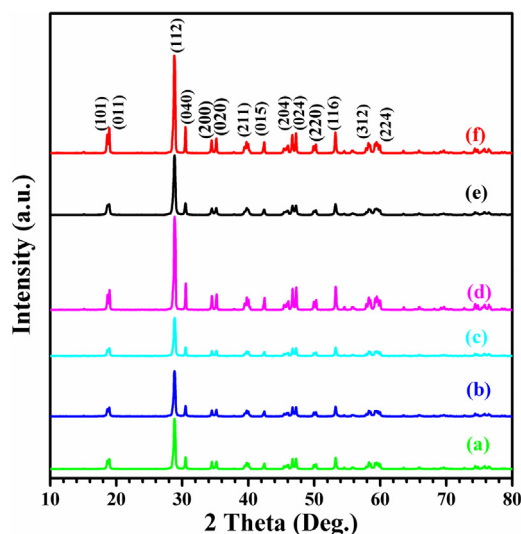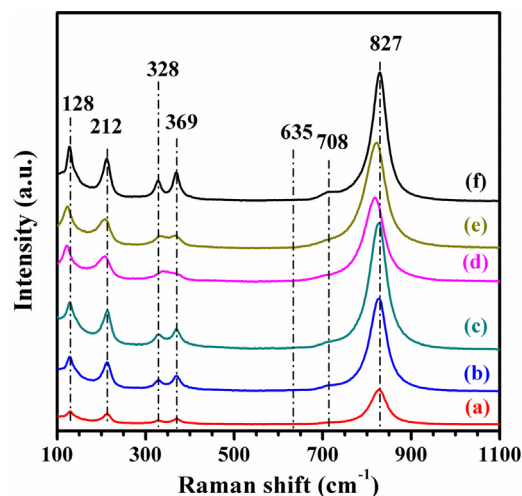
Fig. 1. XRD patterns of (a) 0.18Fe$_2$O$_3$/3DOM BiVO$_4$, (b) 0.97Fe$_2$O$_3$/3DOM BiVO$_4$, (c) 3.40Fe$_2$O$_3$/3DOM BiVO$_4$, (d) 0.92Fe$_2$O$_3$/Bulk BiVO$_4$, (e) 3DOM BiVO$_4$, and (f) Bulk BiVO$_4$.

Fig. 2. Laser Raman spectra of (a) 3DOM BiVO$_4$, (b) 0.18Fe$_2$O$_3$/3DOM BiVO$_4$, (c) 0.97Fe$_2$O$_3$/3DOM BiVO$_4$, (d) 3.40Fe$_2$O$_3$/3DOM BiVO$_4$, (e) 0.92Fe$_2$O$_3$/Bulk BiVO$_4$, and (f) Bulk BiVO$_4$.

of the reactant solution was kept at ca. 25 °C using the flowing cool water. An air flow of 30 mL/min was passed through the suspension. 3.0 mL of the suspension was taken out at certain intervals and centrifuged to remove the photocatalyst particles for the analysis of 4-NP concentration. The 4-NP concentration (C_t) after a certain reaction time (t) was monitored by determining the absorbance of the reactant solution at a wavelength of ca. 315 nm on a Shimadzu UV–vis equipment. The conversion ((C_0-C_t)/C_0 × 100%) of 4-NP was used to evaluate the photocatalytic activity.

3. Results and discussion

3.1. Crystal phase composition

Fig. 1 shows the XRD patterns of the Bulk BiVO$_4$, 3DOM BiVO$_4$, xFe$_2$O$_3$/3DOM BiVO$_4$, and 0.92Fe$_2$O$_3$/Bulk BiVO$_4$ samples. By comparing the XRD pattern (JCPDS PDF# 75-1867) of the standard bismuth vanadate sample, one can realize that the loading of Fe$_2$O$_3$ did not lead to any changes in crystal structure, and the BiVO$_4$ in 3DOM BiVO$_4$ and xFe$_2$O$_3$/3DOM BiVO$_4$ as well as in Bulk BiVO$_4$ or 0.92Fe$_2$O$_3$/Bulk BiVO$_4$ possessed a monoclinic crystal structure, as indexed in Fig. 1f. According to the Scherrer equation ($D = K\lambda/\beta\cos(\theta)$, where λ is the X-ray wavelength, β is the full width at half maximum (FWHM) of the (112) plane of BiVO$_4$, and θ is the corresponding diffraction angle), the grain sizes of BiVO$_4$ in the samples were calculated, as summarized in Table 1. The grain sizes of BiVO$_4$ crystallites in all of the samples were in the range of $26 - 29$ nm. No diffraction signals due to the iron oxide phase were observed in the xFe$_2$O$_3$/3DOM BiVO$_4$ or 0.92Fe$_2$O$_3$/Bulk BiVO$_4$ samples, possibly due to the low loadings and good dispersion of Fe$_2$O$_3$ nanoparticles. The higher intensity of XRD peaks of the Bulk BiVO$_4$ and 0.92Fe$_2$O$_3$/Bulk BiVO$_4$ samples than that of the 3DOM BiVO$_4$ and xFe$_2$O$_3$/3DOM BiVO$_4$ samples indicates that the former had better crystallinity than the latter. The crystal structure of monoclinic scheelite-type BiVO$_4$ was also confirmed by the result of Laser Raman studies. Characteristic Raman bands of BiVO$_4$ crystals could be seen from Fig. 2. It is observed that there were seven Raman bands at 128, 212, 328, 369, 635, 708, and 827 cm^{-1} for each of the samples. The signals were Raman bands characteristic of monoclinic BiVO$_4$ [25]. The Raman bands at 128 and 212 cm^{-1} were assignable to the rotation/translation modes of BiVO$_4$; the ones at 328 and 369 cm^{-1} were attributable to the asymmetric and sym-

metric deformation modes of the VO$_4^{3-}$ tetrahedron, respectively; the one at 635 cm^{-1} was ascribable to the asymmetric stretching vibration of the V—O bond; and the ones at 708 and 827 cm^{-1} were due to the stretching vibrations of two different types of V—O bonds. The shifts of Raman bands at 635 and 708 cm^{-1} (V—O stretching vibration) implies that the lower frequency of the Raman stretching bands corresponded to a longer bond length. Such an implication was confirmed by the well-established functional relationship between the Raman stretching frequency and the metal–oxygen bond length in the local structure. However, no Raman bands assignable to Fe$_2$O$_3$ were detected in the BiVO$_4$-supported Fe$_2$O$_3$ samples. No detection of Fe$_2$O$_3$ Raman bands might be due to the lower Fe$_2$O$_3$ loading. Similar result was also reported by Xu et al. [35]. It should be noted that the position and shape of characteristic Raman bands (328, 369, and 827 cm^{-1}) of the BiVO$_4$-supported Fe$_2$O$_3$ samples were different from those of the 3DOM or Bulk BiVO$_4$ support, indicating that the loading of Fe$_2$O$_3$ exerted an effect on the structure of the sample.

### 3.2. Morphology, pore structure, and surface area

Fig. S2 (Supplementary material) shows the SEM images of the as-prepared samples. It is clearly seen that the 3DOM BiVO$_4$ sample displayed a good-quality 3DOM structure (Fig. S2(a–h)). The BiVO$_4$ in Bulk BiVO$_4$ or 0.92Fe$_2$O$_3$/Bulk BiVO$_4$ possessed a leaf-like morphology (Fig. S2(i, j)). The average macropore sizes of the BiVO$_4$ in the samples were in the range of 160–175 nm. After loading of Fe$_2$O$_3$, the 3DOM structure was still retained. Because of low loadings ($x \le 3.40$ wt%), it is hard to identify the Fe$_2$O$_3$ from the BiVO$_4$ support, but the Fe element was detected by the XPS and ICP − AES techniques. Fig. 3 shows the TEM images and SAED patterns of the as-obtained BiVO$_4$ samples. From the high-resolution TEM images (Fig. 3f and h), one can clearly observe the well-resolved lattice fringes, indicating that these BiVO$_4$-based samples possessed good crystallinity. The interplanar spacings (d values) were measured to be 0.310 and 0.465 nm, in good agreement with those (0.311 and 0.467 nm) of the (112) and (011) crystal planes of the standard BiVO$_4$ sample. The observation of multiple bright electron diffraction rings in the SAED patterns (insets of Fig. 3f) suggests that the 0.97Fe$_2$O$_3$/3DOM BiVO$_4$ sample was polycrystalline.

Fig. 4 illustrates the N$_2$ adsorption–desorption isotherms and pore-size distributions of the 3DOM BiVO$_4$ and xFe$_2$O$_3$/3DOM BiVO$_4$ samples, and their textural parameters are summarized in

Table 1
BET surface areas, pore volumes, average crystallite sizes (D_{BiVO_4}), pore sizes, and real Fe_2O_3 loadings of the samples.

Sample	BET surface area[a] (m^2/g)	Pore volume[a] (cm^3/g)	D_{BiVO_4}[b] (nm)	Macropore size[c] (nm)	Mesopore size[a] (nm)	Real Fe_2O_3 loading[d] (wt%)
Bulk BiVO$_4$	3.1	0.004	29	–	–	–
3DOM BiVO$_4$	28.1	0.058	26	165–175	16–30	–
0.18Fe$_2$O$_3$/3DOM BiVO$_4$	24.8	0.119	28	160–170	17–32	0.18
0.97Fe$_2$O$_3$/3DOM BiVO$_4$	19.0	0.084	27	160–170	20–36	0.97
3.40Fe$_2$O$_3$/3DOM BiVO$_4$	18.1	0.069	27	160–170	22–38	3.40
0.92Fe$_2$O$_3$/Bulk BiVO$_4$	3.4	0.009	28	–	–	0.92

[a] Determined by the BET method.
[b] Estimation according to the Scherrer equation using the FWHM of the (112) line of BiVO$_4$.
[c] Estimated according to the SEM images.
[d] Determined by the ICP – AES technique.
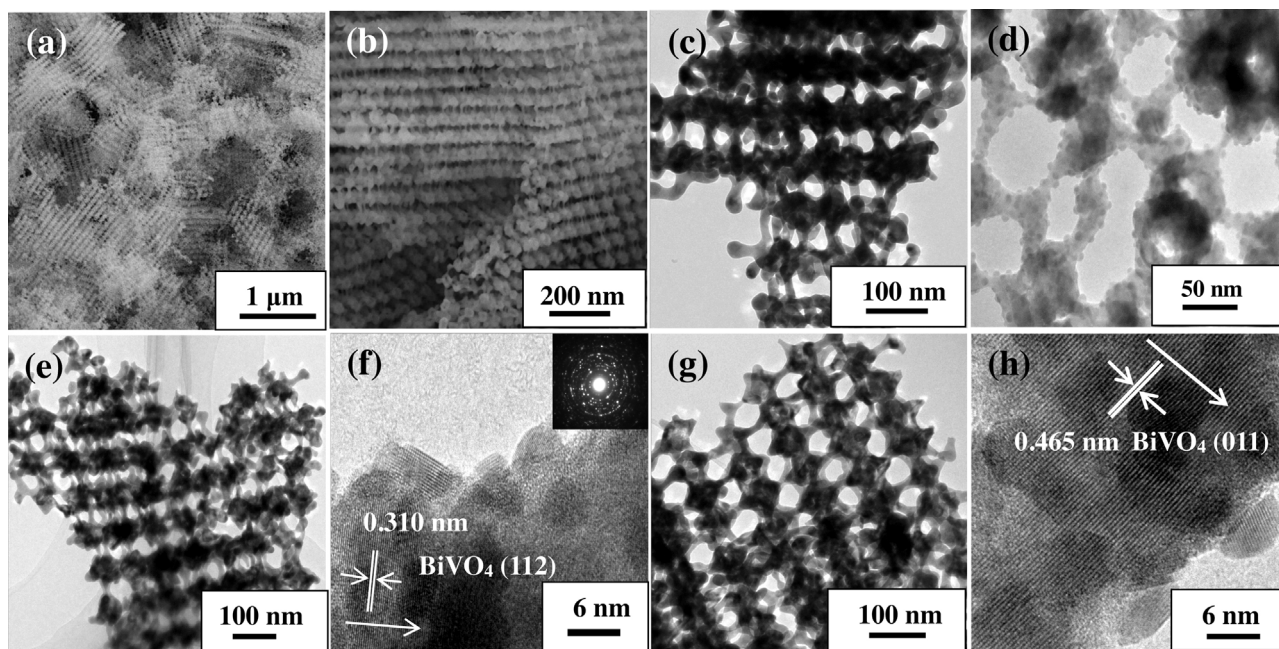
Fig. 3. SEM (a, b) and TEM (c–h) images as well as the SAED pattern (inset) of (a) 3DOM BiVO$_4$, (b, e, f) 0.97Fe$_2$O$_3$/3DOM BiVO$_4$, (c, d) 0.18Fe$_2$O$_3$/3DOM BiVO$_4$, and (g, h) 3.40Fe$_2$O$_3$/3DOM BiVO$_4$.
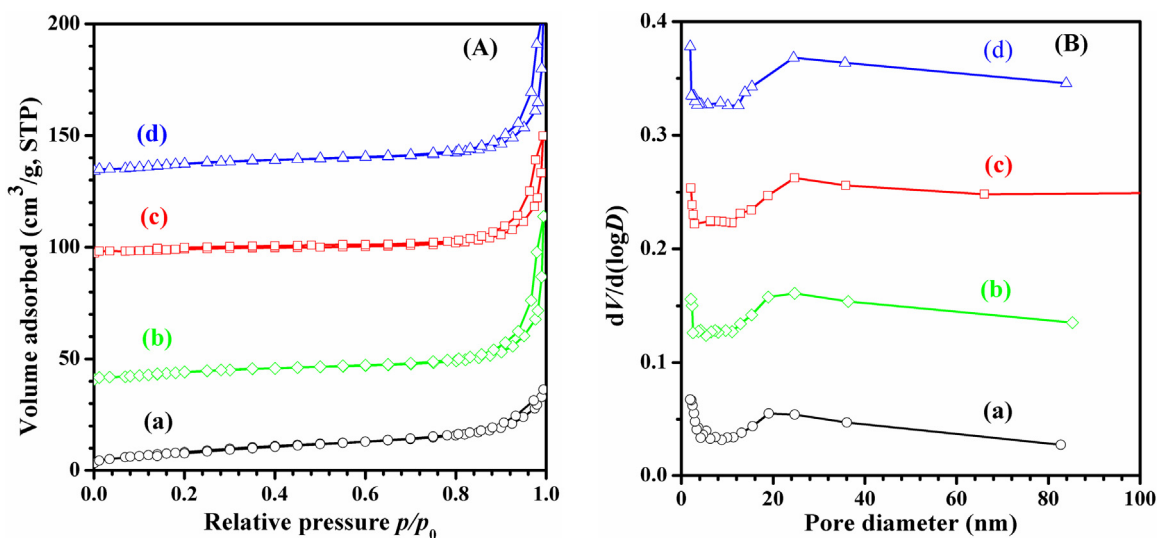
Fig. 4. (A) Nitrogen adsorption–desorption isotherms and (B) pore-size distributions of (a) 3DOM BiVO$_4$, (b) 0.18Fe$_2$O$_3$/3DOM BiVO$_4$, (c) 0.97Fe$_2$O$_3$/3DOM BiVO$_4$, and (d) 3.40Fe$_2$O$_3$/3DOM BiVO$_4$.

Table 1. Each sample displayed a type II adsorption – desorption isotherm with a H3 (p/p_0 = 0.8–1.0) hysteresis loop, indicating that these samples possessed a macroporous structure [36]. Furthermore, the results of SEM and TEM investigations and pore-size
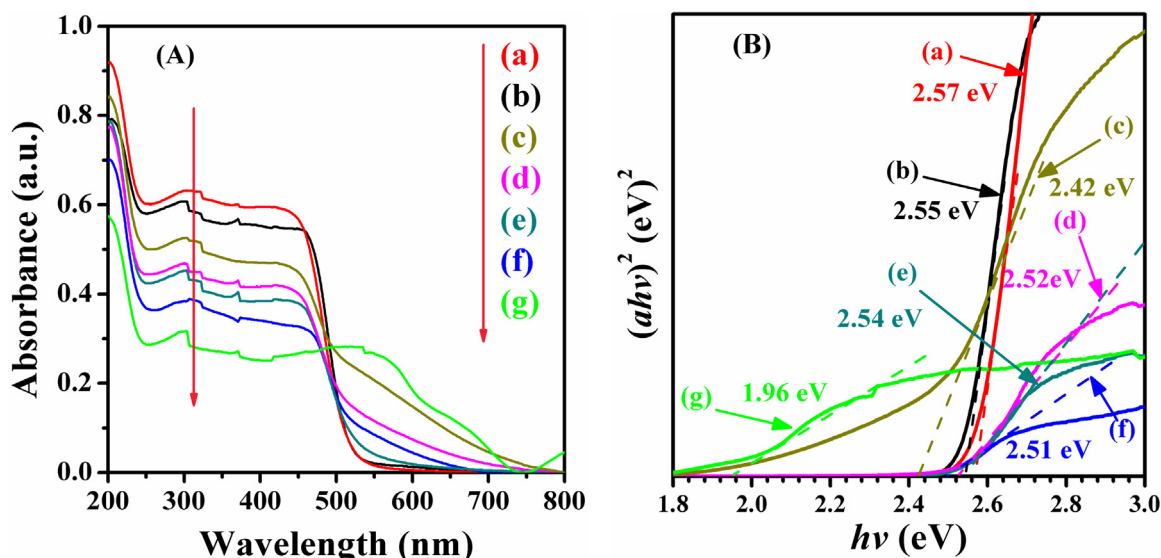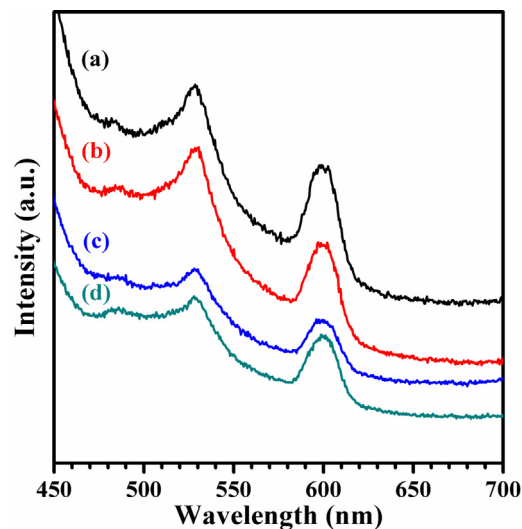
Fig. 5. (A) UV–vis diffuse reflectance spectra and (B) $(\alpha h\nu)^2$ versus $h\nu$ plots of (a) 3DOM $BiVO_4$, (b) Bulk $BiVO_4$, (c) 3.40Fe_2O_3/3DOM $BiVO_4$, (d) 0.97Fe_2O_3/3DOM $BiVO_4$, (e) 0.18Fe_2O_3/3DOM $BiVO_4$, (f) 0.92Fe_2O_3/Bulk $BiVO_4$, and (g) Fe_2O_3.

distributions (Fig. 4B) of the 3DOM $BiVO_4$ and $x$$Fe_2O_3$/3DOM $BiVO_4$ samples also confirm the existence of macropores. Furthermore, there was presence of a small amounts of mesopores and micropores since a wide peak in pore-size distribution scattered from 10 to 60 nm and a drop in dV/d(log D) at a pore size of less than 2 nm appeared. According to the literature [37,38], surface areas of monoclinic $BiVO_4$ obtained via the traditional routes are usually less than 4 m^2/g. Surface areas of Bulk $BiVO_4$ and 0.92Fe_2O_3/Bulk $BiVO_4$ derived from the hydrothermal process were 3.1 and 3.4 m^2/g, respectively. But surface areas and pore volumes of the 3DOM $BiVO_4$ and $x$$Fe_2O_3$/3DOM $BiVO_4$ samples were in the ranges of 18.1–28.7 m^2/g and 0.058–0.119 cm^3/g, respectively, much larger than those of the Bulk $BiVO_4$ and 0.92Fe_2O_3/Bulk $BiVO_4$ samples. The average mesopore sizes of the samples estimated according to the BJH method were in the range of 16–38 nm. These mesopores were formed due to the aggregation of $BiVO_4$ entities. It should be noted that during the Fe_2O_3 loading process that needed impregnation and calcination, some changes in pore structure of the samples would take place and the 3DOM structure decreased in quality, leading to alteration in surface area and pore volume of the samples.
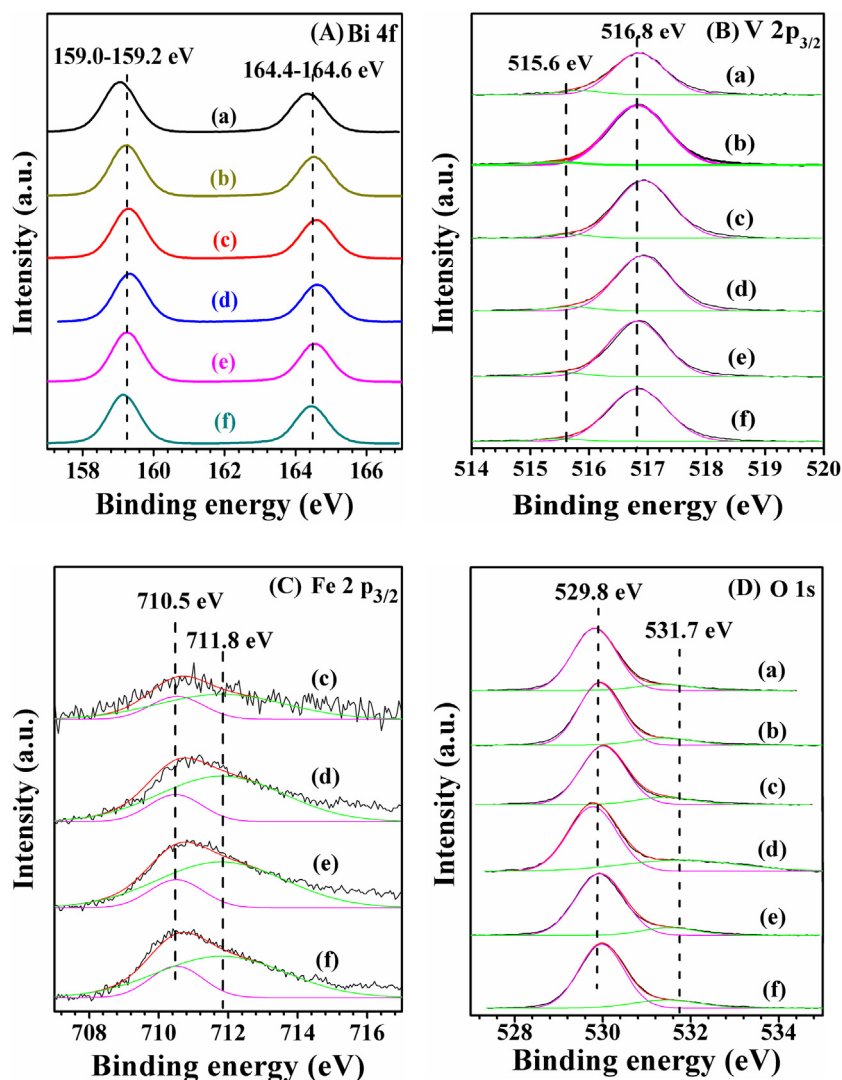
3.3. Light absorption property

Fig. 5A shows the UV–vis DRS of the $BiVO_4$, Fe_2O_3, and $x$$Fe_2O_3$/$BiVO_4$ samples. It is observed all of the samples could absorb the UV and visible light region. However, the $x$$Fe_2O_3$/3DOM or Bulk $BiVO_4$ samples exhibited stronger absorption in the visible-light region than the $BiVO_4$ support. A red shift in absorption edge occurred with the rise in Fe_2O_3 loading, and the 3.40Fe_2O_3/3DOM $BiVO_4$ sample possessed the strongest ability to absorb light. Compared to 3DOM or Bulk $BiVO_4$, the $x$$Fe_2O_3$/3DOM or Bulk $BiVO_4$ samples could be photoexcited to produce more electron–hole pairs under visible light irradiation. It should be noted that each composite had two absorption edges. Figs. 5 B and S3 show the $(\alpha h\nu)^2$ versus $h\nu$ plots of $BiVO_4$ and Fe_2O_3, respectively. The bandgap energies (E_{g1}) of $BiVO_4$ in 3DOM $BiVO_4$, Bulk $BiVO_4$, 0.18Fe_2O_3/3DOM $BiVO_4$, 0.97Fe_2O_3/3DOM $BiVO_4$, 0.92Fe_2O_3/Bulk $BiVO_4$, and 3.40Fe_2O_3/3DOM $BiVO_4$, and Fe_2O_3 were 2.57, 2.55, 2.54, 2.52, 2.51, and 2.42 eV, respectively, which were comparable with those (2.48–2.55 eV) of monoclinic $BiVO_4$ [11]. The E_g of bulk Fe_2O_3 was 1.96 eV, which was close to that (1.90 eV) of Fe_2O_3 [34]. The bandgap energies (E_{g2}) of Fe_2O_3 in

0.18Fe_2O_3/3DOM $BiVO_4$, 0.97Fe_2O_3/3DOM $BiVO_4$, 0.92Fe_2O_3/Bulk $BiVO_4$, and 3.40Fe_2O_3/3DOM $BiVO_4$ were 1.87, 1.86, 1.91, and 1.86 eV, respectively. As compared to bulk Fe_2O_3, the lower E_{g2} of Fe_2O_3 in $x$$Fe_2O_3$/3DOM or Bulk $BiVO_4$ might be related to the high dispersion of Fe_2O_3 on the $BiVO_4$ surface.

Since the PL emission derives from the recombination of photogenerated carriers, a strong PL emission intensity suggests a high recombination possibility of electrons and holes in the sample, which would be unfavorable for improvement in photocatalytic activity [39]. The enhanced photocatalytic activity of the $x$$Fe_2O_3$/3DOM or Bulk $BiVO_4$ samples might be associated with the increased charge separation efficiency. To prove this deduction, PL emission spectra of the typical samples are shown in Fig. 6. The PL emission intensity of the 3DOM $BiVO_4$ and 0.97Fe_2O_3/3DOM $BiVO_4$ samples was much weaker than that of their bulk counterparts; and the 3DOM or Bulk $BiVO_4$-supported Fe_2O_3 samples showed much weaker intensity in PL emission than the 3DOM or Bulk $BiVO_4$ support. This result demonstrates that the undesirable charge recombination process of excited electrons and holes

Fig. 6. Photoluminescence (PL) spectra of (a) Bulk $BiVO_4$, (b) 0.92Fe_2O_3/Bulk $BiVO_4$, (c) 3DOM $BiVO_4$, and (d) 0.97Fe_2O_3/3DOM $BiVO_4$.

Fig. 7. (A) Bi 4f, (B) V 2p$_{3/2}$, (C) Fe 2p$_{3/2}$, and (D) O 1s XPS spectra of (a) Bulk BiVO$_4$, (b) 3DOM BiVO$_4$, (c) 0.18Fe$_2$O$_3$/3DOM BiVO$_4$, (d) 0.97Fe$_2$O$_3$/3DOM BiVO$_4$, (e) 3.40Fe$_2$O$_3$/3DOM BiVO$_4$, and (f) 0.92Fe$_2$O$_3$/Bulk BiVO$_4$.

could be greatly suppressed by making porous BiVO$_4$ (to generate a 3DOM structure) [28] and/or loading Fe$_2$O$_3$ (to form a Fe$_2$O$_3$–BiVO$_4$ heterojunction). Zalfani et al. [40] prepared BiVO$_4$/TiO$_2$ nanocomposites for the photodegradation of rodamine B, and found that the loading of BiVO$_4$ nanoparticles on TiO$_2$ facilitated the efficient charge transfer because of presence of a BiVO$_4$/TiO$_2$ heterojunction. It is well known that a number of factors can influence the performance of a photocatalyst. Although the PL emission intensity can reflect the recombination possibility of electrons and holes, the relationship between the PL emission intensity and photocatalytic performance is still in dispute. In addition to the weakest PL emission intensity, the 0.97Fe$_2$O$_3$/3DOM BiVO$_4$ sample possessed a narrower bandgap energy and the highest adsorbed oxygen species concentration, which also influence its photocatalytic activity. Of course, the photo-Fenton process occurred over the 0.97Fe$_2$O$_3$/3DOM BiVO$_4$ sample also contributed to the improvement in photocatalytic performance. The real reason for the improved catalytic performance of 0.97Fe$_2$O$_3$/3DOM BiVO$_4$ needs to be further investigated in detail.

The 3DOM materials possess a significantly slow photon effect, which could induce the multiple reflections of light and increase the contract between the photon and the material. In this way, light conversion efficiency could be improved. To investigate the

influence of the slow photon effect of 3DOM materials on the photocatalytic performance, the stop-band of 3DOM BiVO$_4$ was calculated through the modified Bragg's law. The equation is shown below:

$$\lambda\,\text{max} = 2\sqrt{\frac{2}{3}}D\sqrt{n_{BiVO4}^2 f + n_{Water}^2(1-f) - \sin^2\theta} \qquad (1)$$

In this equation, λ_{max} is the wavelength of stop-band, D is the pore diameter of 3DOM BiVO$_4$, n_{BiVO4} and n_{Water} are respectively the refractive index of BiVO$_4$ and water, f is the BiVO$_4$ phase volume percentage (generally $f = 0.26$), and θ is the incident angle of light (normally $\theta = 0°$). Therefore, the calculated stop-band of 3DOM BiVO$_4$ was in the range of 478–523 nm. It is noted that the absorption edge of 3DOM BiVO$_4$ was estimated from Fig. 5 to be ca. 485 nm, which fell into the stop-band range of 3DOM BiVO$_4$.
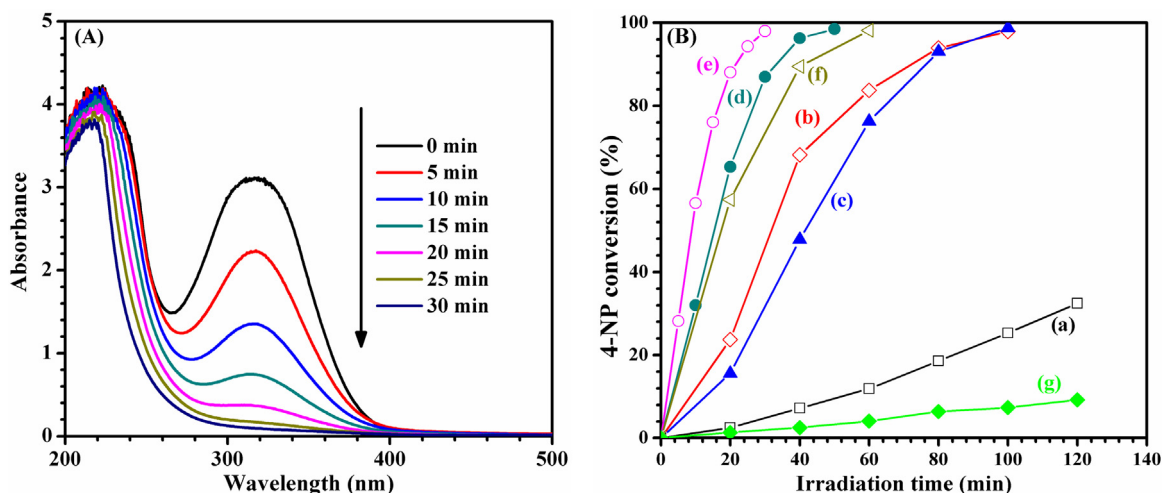
3.4. Surface element composition, metal oxidation state, and adsorbed oxygen species

XPS is an effective technique to investigate the surface element composition, metal oxidation state, and adsorbed oxygen species of a catalyst. Fig. 7 illustrates the Bi 4f, V 2p$_{3/2}$, Fe 2p$_{3/2}$, and O 1s XPS spectra of the samples. There were two symmetric peaks of Bi

Table 2
Surface element compositions, bandgap energies (E_g), rate constants (k), and correlation coefficients (R) of the samples.

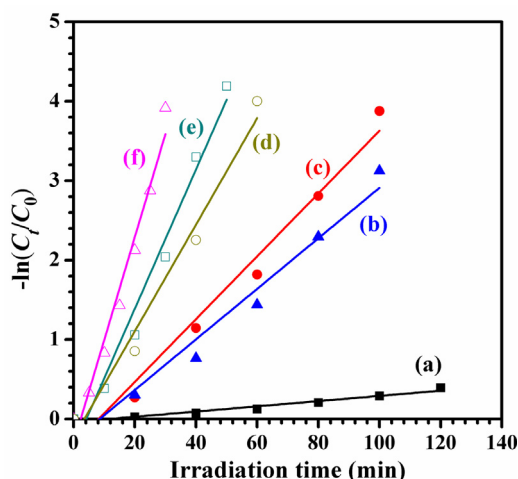| Sample	Surface element composition			Bandgap energy (eV)		k (min^{-1})	R
	V^{4+}/V^{5+} molar ratio	Fe^{2+}/Fe^{3+} molar ratio	O_{ads}/O_{latt} molar ratio	E_{g1}	E_{g2}		
Bulk BiVO$_4$	0.031	–	0.124	2.55	–	0.0033	0.9819
3DOM BiVO$_4$	0.042	–	0.138	2.57	–	0.0318	0.9849
0.18Fe$_2$O$_3$/3DOM BiVO$_4$	0.055	0.385	0.153	2.54	1.86	0.0876	0.9868
0.97Fe$_2$O$_3$/3DOM BiVO$_4$	0.064	0.255	0.186	2.52	1.87	0.1295	0.9874
3.40Fe$_2$O$_3$/3DOM BiVO$_4$	0.049	0.261	0.140	2.42	1.86	0.0670	0.9889
0.92Fe$_2$O$_3$/Bulk BiVO$_4$	0.045	0.318	0.149	2.51	1.91	0.0395	0.9878

Fig. 8. (A) UV–vis absorbance spectra of 0.97Fe$_2$O$_3$/3DOM BiVO$_4$ and (B) 4-NP concentration versus visible light illumination time over (a) Bulk BiVO$_4$, (b) 0.92Fe$_2$O$_3$/Bulk BiVO$_4$, (c) 3DOM BiVO$_4$, (d) 0.18Fe$_2$O$_3$/3DOM BiVO$_4$, (e) 0.97Fe$_2$O$_3$/3DOM BiVO$_4$, (f) 3.40Fe$_2$O$_3$/3DOM BiVO$_4$, and (g) no catalyst in the presence of 0.6 mL H$_2$O$_2$ for the degradation of 4-NP aqueous solution (C_0 = 0.4 mmol/L) under visible light ($\lambda \geq 400$ nm) illumination.

4f$_{7/2}$ and Bi 4f$_{5/2}$ at BE = 159.0–159.2 and 164.4–164.6 eV (Fig. 7A), respectively, which were characteristic of surface Bi^{3+} species [41]. From Fig. 7B, one can see an asymmetrical V 2p$_{3/2}$ XPS signal of each sample that could be decomposed to two components at BE = 515.6 and 516.8 eV, assignable to the surface V^{4+} and V^{5+} species [25], respectively. As summarized in Table 2, the surface V$^{4+}/$V^{5+} molar ratio increased after the loading of Fe$_2$O$_3$ on the BiVO$_4$ surface. The surface V$^{4+}/$V^{5+} molar ratio (0.042) of the 3DOM BiVO$_4$ sample was higher than that (0.031) of the Bulk BiVO$_4$ sample. Among the xFe$_2$O$_3$/3DOM or Bulk BiVO$_4$ samples, 0.97Fe$_2$O$_3$/3DOM BiVO$_4$ possessed the highest surface V$^{4+}/$V^{5+} molar ratio (0.064), indicating that there was a more amount of oxygen vacancies in the 0.97Fe$_2$O$_3$/3DOM BiVO$_4$ sample. As for the Fe 2p$_{3/2}$ XPS spectra of the Fe$_2$O$_3$-loaded samples, there was an asymmetrical signal that could be decomposed into two components at BE = 710.5 and 711.8 eV (Fig. 7C), attributable to the surface Fe^{2+} and Fe^{3+} species [34], respectively. The surface Fe$^{2+}/$Fe^{3+} molar ratio (0.255) was the lowest on the surface of 0.97Fe$_2$O$_3$/3DOM BiVO$_4$, meaning that a more amount of oxygen vacancies existed in Fe$_2$O$_3$ of the 0.97Fe$_2$O$_3$/3DOM BiVO$_4$ sample. The asymmetrical O 1s XPS peak of each sample was decomposed to two components at BE = 529.8 and 531.7 eV (Fig. 7D), ascribable to the surface lattice oxygen (O$_{latt}$) and adsorbed oxygen (O$_{ads}$, e.g., O$_2^-$, O$_2^{2-}$ or O$^-$) species [42], respectively. The O$_{ads}/$O$_{latt}$ molar ratio of xFe$_2$O$_3$/3DOM or Bulk BiVO$_4$ increased after Fe$_2$O$_3$ loading. Since the O 1s XPS spectra were recorded without exposure to the air after the samples were pretreated in O$_2$ at 450 °C, the adsorbed water and carbonate species on the sample surface were minimized. In other word, the adsorbed oxygen species were mainly the O$_2^-$, O$_2^{2-}$ or O$^-$ species. On the basis of the electroneutrality principle, the higher the V^{4+} or Fe^{2+} species concentration, the higher is the amount of oxygen vacancy density in BiVO$_4$ or Fe$_2$O$_3$. From Table 2, one can find the chang-

ing trend in O$_{ads}/$O$_{latt}$ molar ratio was in agreement with that in surface V$^{4+}/$V^{5+} or Fe$^{2+}/$Fe^{3+} molar ratio. According to the literature [43], the rise in O$_{ads}$ species concentration would be beneficial for enhancement in catalytic performance for oxidation of organics.

3.5. Photocatalytic performance

The characteristic absorption band of 4-NP at a wavelength of 315 nm was used to monitor the photocatalytic degradation process. Since there was only a small amount of Fe$_2$O$_3$ in the photocatalytic system, the absorbance of the reactant solution nearly remained unchanged after 2 h of adsorption in the dark. Therefore, we think that the Fenton oxidation could be ignored during the adsorption process. Fig. 8A illustrates the UV–vis spectra of the samples for 4-NP degradation over 0.97Fe$_2$O$_3$/3DOM BiVO$_4$ under visible light irradiation. Obviously, the characteristic absorption band of 4-NP at 315 nm decreased monotonously with irradiation time, indicating that 4-NP was photodegraded. Fig. 8B shows the photocatalytic activities of the as-prepared samples for 4-NP (C_0 = 0.4 mmol/L) degradation as well as the photolysis without catalyst in the presence of 0.6 mL H$_2$O$_2$ under visible light illumination. After 2 h of visible light irradiation, 4-NP conversion in the direct photolysis was only 10%, indicating that the photolysis of 4-NP was insignificant. Only 40% 4-NP could be removed over Bulk BiVO$_4$ after 2 h of visible light illumination. However, the time for complete removal of 4-NP was 30, 50, 60, and 100 min over the 0.97Fe$_2$O$_3$/3DOM BiVO$_4$, 0.18Fe$_2$O$_3$/3DOM BiVO$_4$, 3.40Fe$_2$O$_3$/3DOM BiVO$_4$, 3DOM BiVO$_4$, and 0.92Fe$_2$O$_3$/Bulk BiVO$_4$ photocatalysts, respectively. In order to verify the synergistic effect of the heterojunction between Fe$_2$O$_3$ and BiVO$_4$, we evaluated the photocatalytic activities of single Fe$_2$O$_3$ and the mechanically mixed (1.0 wt% Fe$_2$O$_3$ + 3DOM BiVO$_4$) sample for 4-

Fig. 9. Kinetic curves obtained over (a) Bulk BiVO$_4$, (b) 3DOM BiVO$_4$, (c) 0.92Fe$_2$O$_3$/Bulk BiVO$_4$, (d) 3.40Fe$_2$O$_3$/3DOM BiVO$_4$, (e) 0.18Fe$_2$O$_3$/3DOM BiVO$_4$, and (f) 0.97Fe$_2$O$_3$/3DOM BiVO$_4$ for the degradation of 4-NP.

NP degradation, as shown in Fig. S4. It is observed that the time for complete removal of 4-NP was 170 and 90 min over the Fe$_2$O$_3$ and 1.0 wt% Fe$_2$O$_3$ + 3DOM BiVO$_4$ samples, respectively. That is to say, the excellent performance of 0.97Fe$_2$O$_3$/3DOM BiVO$_4$ was not from the contribution of Fe$_2$O$_3$, and the improved photocatalytic performance was mainly due to the synergistic effect of the Fe$_2$O$_3$–3DOM BiVO$_4$ heterojunction. It has been reported that formation of a porous structure can not only increase the surface area but also enhance the light capturing ability, thus improving the photocatalytic efficiency of the sample [28–30]. Therefore, it is concluded the excellent photocatalytic performance of 3DOM BiVO$_4$ is related to the existence of the slow photon effect of the 3DOM material. It should be noted that no other absorption peaks ascribable to intermediates formed during the photocatalytic process were detected over all of the as-fabricated samples under visible light illumination. Therefore, the photocatalytic activities calculated according to the alteration in absorbance of 4-NP in the suspension were reliable.

The photocatalytic 4-NP degradation kinetics over different photocatalysts was also investigated. The photocatalytic degradation of 4-NP over the samples obeyed a pseudo first-order mechanism, so called the Langmuir–Hinshelwood (L–H) mecha-
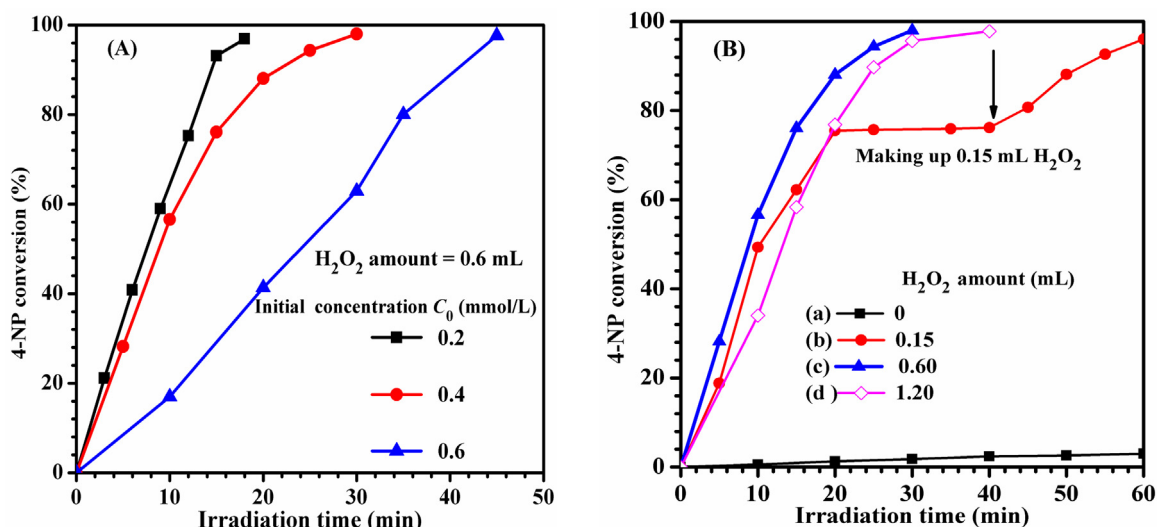
nism. According to the L–H mechanism, the relationship between the degradation rate (r) and organic pollutant concentration (C_t) is as follows [44,45]:

$$r = -dC_t/dt = kC_t \tag{2}$$

where k is the apparent first-order rate constant (min^{-1}). Fig. 9 shows the linear plots of $-\ln(C_t/C_0)$ versus irradiation time, and the rate constant and correlation coefficient (R) are given in Table 2. The k value obtained over the 3DOM BiVO$_4$ sample was estimated to be 0.0318 min^{-1}, which was about 10 times higher than that (0.0033 min^{-1}) obtained over the nonporous Bulk BiVO$_4$ sample. After the loading of Fe$_2$O$_3$ on 3DOM BiVO$_4$, the k value increased, with the 0.97Fe$_2$O$_3$/3DOM BiVO$_4$ sample showing the highest rate constant (0.1295 min^{-1}).

Fig. 10A shows the effect of initial 4-NP concentration on the photocatalytic activity of the 0.97Fe$_2$O$_3$/3DOM BiVO$_4$ sample in the presence of H$_2$O$_2$ (0.6 mL) under visible light irradiation. It can be seen that the photocatalytic activity decreased with the rise in initial 4-NP concentration from C_0 = 0. 2 to 0.4 and further to 0.6 mmol/L, the time required for achieving a ca. 98% 4-NP conversion was from 18 to 30 and further to 45 min, respectively. Juang and coworkers [46] reported similar results in the UV/TiO$_2$ system for the photocatalytic degradation of phenol.

To examine the effect of H$_2$O$_2$ amount on the photocatalytic activity of the best-performing 0.97Fe$_2$O$_3$/3DOM BiVO$_4$ sample, different initial H$_2$O$_2$ amounts were added to the reaction solution. From Fig. 10B, one can observe that 4-NP conversion was very low (5%) in the absence of H$_2$O$_2$ after 2 h of visible light illumination. However, the 4-NP degradation efficiency increased significantly in the presence of 0.6 mL of H$_2$O$_2$. When the H$_2$O$_2$ amount was 0.15 mL, 4-NP conversion increased quickly in the initial 20 min (approximate 75% 4-NP was converted). However, 4-NP conversion almost maintained unchanged after 20 min of reaction. In order to confirm the role of H$_2$O$_2$ on the photocatalytic degradation of 4-NP, 0.15 mL of H$_2$O$_2$ was made up to the system after 40 min of reaction. It is observed that 4-NP conversion increased again. This result demonstrates that 0.15 mL of H$_2$O$_2$ was insufficient for the total degradation of 4-NP. H$_2$O$_2$ is a kind of electron scavenger that can facilitate the generation of reactive •OH species. When the amount of H$_2$O$_2$ was increased to 1.20 mL, the photocatalytic activity declined slightly (97% 4-NP conversion was achieved within 40 min of photocatalytic reaction), as compared to the case of 0.6 mL H$_2$O$_2$ addition. The result suggests that an excessive amount of

Fig. 10. Effects of initial 4-NP concentration and H$_2$O$_2$ amount on the photocatalytic activity of the 0.97Fe$_2$O$_3$/3DOM BiVO$_4$ sample for the degradation of 4-NP under visible light illumination.

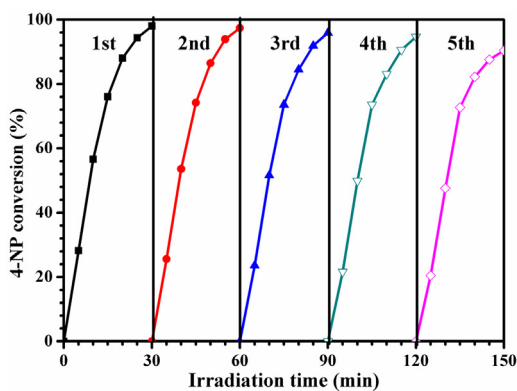**Fig. 11.** Recycling runs of 0.97Fe$_2$O$_3$/3DOM BiVO$_4$ for the degradation of 4-NP (C_0 = 0.4 mmol/L) under visible light irradiation.

Fig. 12. Schematic illustration of bandgap energy and charge carrier migration and separation on the xFe$_2$O$_3$/3DOM BiVO$_4$ heterojunction structure under visible light irradiation.

H$_2$O$_2$ was unfavorable for improvement in degradation activity. It has been proposed that excessive H$_2$O$_2$ could convert reactive species into inactive radicals or molecules [47]. Therefore, an optimal amount of H$_2$O$_2$ would be needed for the maximal conversion of 4-NP.

It is well known that the stability and reusability of a photocatalyst are very important for practical applications. Therefore, we carried out the recycling runs of 0.97Fe$_2$O$_3$/3DOM BiVO$_4$ for photocatalytic degradation of 4-NP within 30 min of visible light illumination. As shown in Fig. 11, ca. 90% 4-NP conversion was maintained after five runs, indicating that the 0.97Fe$_2$O$_3$/3DOM BiVO$_4$ sample exhibited good photocatalytic stability. Since Fe$_2$O$_3$ participates in an oxidation–reduction recycle, there should be no Fe loss during the recycle process. Rtimi et al. [48] reported FeO$_x$-TiO$_2$ photocatalytic films for the degradation of indole, and found that only 0.5 ppb Fe leaching was detected. Furthermore, the 0.97Fe$_2$O$_3$/3DOM BiVO$_4$ sample exhibited good photocatalytic stability after five reaction runs, confirming that the leaching of Fe was negligible. Therefore, the Fe leaching was minimal in our photocatalytic system.

3.6. Photocatalytic mechanism

By comparing the results of our present study and other researchers' investigations [49], one can realize that the xFe$_2$O$_3$/3DOM BiVO$_4$ photocatalysts exhibited better photocatalytic performance for the degradation of 4-NP under visible light illumination. We propose the possible reaction mechanism, as illustrated in Fig. 12. The conduction band (E_{CB}) and valence band (E_{VB}) edges of a semiconductor can be calculated by the two following equations [31,50]:

$$E_{CB} = \chi - E_c - 0.5E_g \qquad (3)$$

$$E_{VB} = E_g + E_{CB} \qquad (4)$$

where χ is the absolute electronegativity of the semiconductor, E_c is the energy of free electrons on the hydrogen scale (ca. 4.5 eV), and E_g is the bandgap energy. Based on the UV–vis DRS data measured above, the bandgap energies of 3DOM BiVO$_4$ and Fe$_2$O$_3$ were about 2.57 and 1.96 eV, respectively. According to the results reported by Xu et al. [51], the absolute electronegativity (χ) of Fe$_2$O$_3$ and BiVO$_4$ was 5.88 and 6.04 eV, respectively. The calculated E_{CB} and E_{VB} values of 3DOM BiVO$_4$ were 0.26 and 2.83 eV, and those of Fe$_2$O$_3$ were 0.40 and 2.36 eV, respectively. Fe$_2$O$_3$ and BiVO$_4$ could be excited to simultaneously generate electrons (e$^-$) and holes (h$^+$) under visible light irradiation. For the xFe$_2$O$_3$/3DOM BiVO$_4$ heterojunction structure, due to the conduction band position of Fe$_2$O$_3$ was more anodic than that of BiVO$_4$, the excited electrons on the conduction band of BiVO$_4$ could be transferred
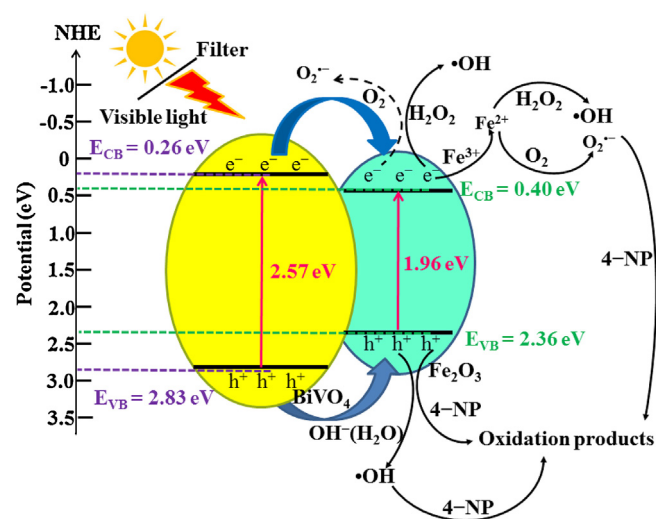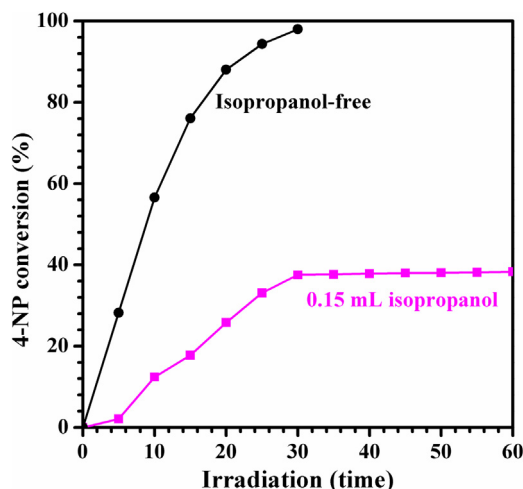
to the conduction band of Fe$_2$O$_3$, thus separating the electrons and holes generated in the xFe$_2$O$_3$/3DOM BiVO$_4$ samples. The results of PL investigations also confirm that recombination of the photogenerated electron/hole pairs was greatly suppressed after the loading of Fe$_2$O$_3$ on 3DOM BiVO$_4$.
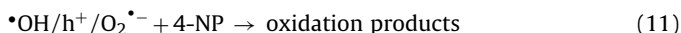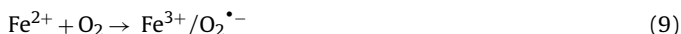
Due to the E_{CB} of Fe$_2$O$_3$ was more positive than that of O$_2$/O$_2^{\bullet-}$ (-0.33 eV versus NHE) [52], the electrons could not react with oxygen molecules to form superoxide radical anions (O$_2^{\bullet-}$). However, the E_{VB} of Fe$_2$O$_3$ was more positive than that of $^{\bullet}$OH/OH$^-$ (+1.99 eV versus NHE) and $^{\bullet}$OH/H$_2$O (+2.27 eV versus NHE) [28,53], thus residual photoexcited holes on the valence band could readily oxidize the adsorbed H$_2$O molecules or the surface hydroxyl (OH$^-$) to generate the hydroxyl radical ($^{\bullet}$OH), which was highly active for the photocatalytic oxidation of 4-NP. In addition, hydroxyl radicals also can be generated by the photo-Fenton process. When the xFe$_2$O$_3$/3DOM BiVO$_4$ catalysts are exposed to visible light, Fe^{3+} can be reduced to Fe^{2+} by the electrons in CB of Fe$_2$O$_3$ and transferred from the CB of BiVO$_4$. Then Fe^{2+} can react with H$_2$O$_2$ to form hydroxyl radicals. Furthermore, Fe^{2+} also can activate O$_2$ molecules adsorbed on the catalyst surface into O$_2^{\bullet-}$ [54,55].

In order to investigate the main actives species in the photocatalytic process, we carried out the $^{\bullet}$OH-trapping experiment over the 0.97Fe$_2$O$_3$/3DOM BiVO$_4$ sample, as shown in Fig. 13. Such an experiment was to investigate the role of $^{\bullet}$OH using the isopropanol as $^{\bullet}$OH quencher [56,57]. The addition of 0.15 mL isopropanol caused a significant decrease in photocatalytic efficiency: 4-NP conversion decreased from 97 to 37% within 30 min of visible light illumination. This result suggests that $^{\bullet}$OH was mainly the active species for photocatalytic 4-NP degradation. Furthermore, although the holes and O$_2^{\bullet-}$ could directly react with 4-NP to produce intermediates or CO$_2$ and H$_2$O, a higher fraction of the holes on the VB of BiVO$_4$ were transferred to the VB of Fe$_2$O$_3$ and the generated O$_2^{\bullet-}$ was in minority. Hence, the holes and O$_2^{\bullet-}$ might play a secondary role in photocatalyzing the degradation of 4-NP. On the basis of the results discussed above, we believe that the main active species in our reaction system were the $^{\bullet}$OH species. The possible photocatalytic reaction mechanism over the xFe$_2$O$_3$/3DOM BiVO$_4$ photocatalysts might be as follows:

$$Fe_2O_3/BiVO_4 + h\nu \rightarrow e^- + h^+ \qquad (5)$$

$$e^- + H_2O_2 \rightarrow {}^{\bullet}OH + OH^- \qquad (6)$$

$$e^- + Fe^{3+} \rightarrow Fe^{2+} \qquad (7)$$

Fig. 13. Effect of isopropanol on the photocatalytic activity of the 0.97Fe$_2$O$_3$/3DOM BiVO$_4$ sample for the degradation of 4-NP under visible light illumination.

$$Fe^{2+} + H_2O_2 \rightarrow Fe^{3+} + {}^{\bullet}OH + OH^- \tag{8}$$

$$Fe^{2+} + O_2 \rightarrow Fe^{3+}/O_2^{\bullet -} \tag{9}$$

$$h^+ + H_2O(OH^-) \rightarrow {}^{\bullet}OH \tag{10}$$

$${}^{\bullet}OH/h^+/O_2^{\bullet -} + 4\text{-}NP \rightarrow \text{oxidation products} \tag{11}$$

4. Conclusions

High-quality 3DOM-structured monoclinic BiVO$_4$ and its supported Fe$_2$O$_3$ photocatalysts were prepared using the ascorbic acid-assisted PMMA-templating and incipient wetness impregnation methods, respectively. The Fe$_2$O$_3$ nanoparticles were highly dispersed on the surface of 3DOM BiVO$_4$. The xFe$_2$O$_3$/3DOM BiVO$_4$ samples showed much better photocatalytic activities than the 3DOM BiVO$_4$ sample, with 0.97Fe$_2$O$_3$/3DOM BiVO$_4$ performing the best for 4-NP degradation under visible light illumination (98% 4-NP conversion was achieved in the presence of 0.6 mL H$_2$O$_2$ within 0.5 h of reaction). H$_2$O$_2$ addition was essential in promoting the photocatalytic process, in which the ${}^{\bullet}$OH generated via the reaction of photoinduced electrons and H$_2$O$_2$ was the main active species. The 0.97Fe$_2$O$_3$/3DOM BiVO$_4$ sample exhibited excellent photocatalytic stability. Kinetic studies reveal that the photocatalytic 4-NP degradation obeyed a pseudo-first-order reaction mechanism and the rate constants (0.0876–0.1295 min^{-1}) obtained over xFe$_2$O$_3$/3DOM BiVO$_4$ were much higher than those (0.0033–0.0395 min^{-1}) obtained over 3DOM or Bulk BiVO$_4$ and Fe$_2$O$_3$/Bulk BiVO$_4$, with the 0.97Fe$_2$O$_3$/3DOM BiVO$_4$ sample showing the highest rate constant. It is concluded that the unique porous architecture, high surface area, Fe$_2$O$_3$–BiVO$_4$ heterojunction, good light-harvesting capacity, high adsorbed oxygen species concentration, and excellent separation efficiency of photoinduced electrons and holes as well as the photo-Fenton degradation process were responsible for the enhanced photocatalytic performance of 0.97Fe$_2$O$_3$/3DOM BiVO$_4$. We believe that such Fe$_2$O$_3$/3DOM BiVO$_4$ composite materials would have potential applications for the treatments of organics-containing wastewater.

Acknowledgements

Appendix A. Supplementary data

Supplementary data associated with this article can be found, in the online version, at http://dx.doi.org/10.1016/j.apcatb.2016.09.069.

References

[1] A. Hernández-Gordillo, A.G. Romero, F. Tzompantzi, R. Gómez, Appl. Catal. B 144 (2014) 507–513.
[2] B.X. Li, Y.G. Hao, X.K. Shao, H.D. Tang, T. Wang, J.B. Zhu, S.L. Yan, J. Catal. 329 (2015) 368–378.
[3] A.D. Paola, G. Marcì, L. Palmisano, M. Schiavello, K. Uosaki, S. Ikeda, B. Ohtani, J. Phys. Chem. B 106 (2002) 637–645.
[4] R. Vinu, G. Madras, Environ. Sci. Technol. 42 (2008) 913–919.
[5] X.T. Shen, L.H. Zhu, G.X. Liu, H.W. Yu, H.Q. Tang, Environ. Sci. Technol. 42 (2008) 1687–1692.
[6] Y. Ma, X.L. Wang, Y.S. Jia, X.B. Chen, H.X. Han, C. Li, Chem. Rev. 114 (2014) 9987–10043.
[7] W.Z. Yin, W.Z. Wang, L. Zhou, S.M. Sun, L. Zhang, J. Hazard. Mater. 173 (2010) 194–199.
[8] R.B. Jiang, B.X. Li, C.H. Fang, J.F. Wang, Adv. Mater. 26 (2014) 5274–5309.
[9] S.M. Yoo, S.B. Rawal, J.E. Lee, J. Kim, H.-Y. Ryu, D.-W. Park, W.I. Lee, Appl. Catal. A 499 (2015) 47–54.
[10] Y. Park, K.J. McDonald, K.S. Choi, Chem. Soc. Rev. 42 (2013) 2321–2337.
[11] W. Liu, Y.Q. Yu, L.X. Cao, G. Su, X.Y. Liu, L. Zhang, Y.G. Wang, J. Hazard. Mater. 181 (2010) 1102–1108.
[12] G.S. Li, D.Q. Zhang, J.C. Yu, Chem. Mater. 20 (2008) 3983–3992.
[13] R.G. Li, H.X. Han, F.X. Zhang, D.E. Wang, C. Li, Energy Environ. Sci. 7 (2014) 1369–1376.
[14] L. Chen, S.F. Yin, R. Huang, Q. Zhang, S.L. Luo, C.T. Au, CrystEngComm 14 (2012) 4217–4222.
[15] A. Kudo, K. Omori, H. Kato, J. Am. Chem. Soc. 121 (1999) 11459–11467.
[16] S. Obregón, A. Caballero, G. Colón, Appl. Catal. B 117–118 (2012) 59–66.
[17] S.W. Cao, Z. Yin, J. Barber, F.Y.C. Boey, S.C.J. Loo, C. Xue, ACS Appl. Mater. Interfaces 4 (2012) 418–423.
[18] L. Ge, Mater. Chem. Phys. 107 (2008) 465–470.
[19] W.Q. Cui, W.J. An, L. Liu, J.S. Hu, Y.H. Liang, J. Hazard. Mater. 280 (2014) 417–427.
[20] S. Kohtani, K. Yoshida, T. Maekawa, A. Iwase, A. Kudo, H. Miyabe, R. Nakagaki, Phys. Chem. Chem. Phys. 10 (2008) 2986–2992.
[21] M.C. Long, W.M. Cai, J. Cai, B.X. Zhou, X.Y. Chai, Y.H. Wu, J. Phys. Chem. B 110 (2006) 20211–20216.
[22] Y. Shi, H.Y. Li, L. Wang, W. Shen, H.Z. Chen, ACS Appl. Mater. Interfaces 4 (2012) 4800–4806.
[23] L.L. Peng, T.F. Xie, Y.C. Lu, H.M. Fan, D.J. Wang, Phys. Chem. Chem. Phys. 12 (2010) 8033–8041.
[24] M. Srinivasan, T. White, Environ. Sci. Technol. 41 (2007) 4405–4409.
[25] Y.X. Liu, H.X. Dai, J.G. Deng, L. Zhang, C.T. Au, Nanoscale 4 (2012) 2317–2325.
[26] Y. Wang, H.X. Dai, J.G. Deng, Y.X. Liu, Z.X. Zhao, X.W. Li, H. Arandiyan, Chem. Eng. J. 226 (2013) 87–94.
[27] S.M. Sun, W.Z. Wang, L. Zhang, J. Mater. Chem. 22 (2012) 19244–19249.
[28] B. Lin, G.D. Yang, B.L. Yang, Y.X. Zhao, Appl. Catal. B 198 (2016) 276–285.
[29] Y. Chang, K. Yu, C.X. Zhang, R. Li, P.Y. Zhao, L.L. Lou, S.X. Liu, Appl. Catal. B 176–177 (2015) 363–373.
[30] K. Yu, C.X. Zhang, Y. Chang, Y.J. Feng, Z.Q. Yang, T. Yang, L.L. Lou, S.X. Liu, Appl. Catal. B 200 (2017) 514–520.
[31] S.H. Xie, H.X. Dai, J.G. Deng, Y.X. Liu, H.G. Yang, Y. Jiang, W. Tan, A.S. Ao, G.S. Guo, Nanoscale 5 (2013) 11207–11219.
[32] S.H. Xie, H.X. Dai, J.G. Deng, Y.X. Liu, H.G. Yang, W. Han, H. Arandiyan, G.S. Guo, J. Hazard. Mater. 279 (2014) 392–401.
[33] H.N. Li, L. Zhang, H.X. Dai, H. He, Inorg. Chem. 48 (2009) 4421–4434.
[34] R.Z. Zhang, H.X. Dai, Y.C. Du, L. Zhang, J.G. Deng, Y.S. Xia, Z.X. Zhao, X. Meng, Y.X. Liu, Inorg. Chem. 50 (2011) 2534–2544.
[35] J. Xu, W.Z. Wang, J. Wang, Y.J. Liang, Appl. Surf. Sci. 349 (2015) 529–537.
[36] H.W. Yan, C.F. Blanford, B.T. Holland, W.H. Smyrl, A. Stein, Chem. Mater. 12 (2000) 1134–1141.
[37] D.N. Ke, T.Y. Peng, L. Ma, P. Cai, K. Dai, Inorg. Chem. 48 (2009) 4685–4691.
[38] M.L. Guan, D.K. Ma, S.W. Hu, Y.J. Chen, S.M. Huang, Inorg. Chem. 50 (2011) 800–805.
[39] N. Zhang, S.Q. Liu, X.Z. Fu, Y.J. Xu, J. Phys. Chem. B 115 (2011) 9136–9145.
[40] M. Zalfani, B.V.D. Schueren, Z.Y. Hu, J.C. Rooke, R. Bourguiga, M. Wu, Y. Li, G.V. Tendeloo, B.L. Su, J. Mater. Chem. A 3 (2015) 21244–21256.
[41] S. Poulston, N.J. Price, C. Weeks, M.D. Allen, P. Parlett, M. Steinberg, M. Bowker, J. Catal. 178 (1998) 658–667.
[42] Y.X. Liu, H.X. Dai, J.G. Deng, X.W. Li, Y. Wang, H. Arandiyan, S.H. Xie, H.G. Yang, G.S. Guo, J. Catal. 305 (2013) 146–153.
[43] S.H. Xie, J.G. Deng, S.M. Zang, H.G. Yang, G.S. Guo, H. Arandiyan, H.X. Dai, J. Catal. 322 (2015) 38–48.
[44] I.K. Konstantinou, T.A. Albanis, Appl. Catal. B 49 (2004) 1–14.
[45] S.Y. Chai, Y.J. Kim, M.H. Jung, A.K. Chakraborty, D. Jung, W.I. Lee, J. Catal. 262 (2009) 144–149.
[46] C.H. Chiou, C.Y. Wu, R.S. Juang, Chem. Eng. J. 139 (2008) 322–329.

[47] G. Granados-Oliveros, E.A. Páez-Mozo, F.M. Ortega, C. Ferronato, J.-M. Chovelon, Appl. Catal. B 89 (2009) 448–454.

[48] S. Rtimi, M. Robyr, C. Pulgarin, J.C. Lavanchy, J. Kiwi, J. Catal. 342 (2016) 184–192.

[49] G.P. Yao, J. Li, Y. Luo, W.J. Sun, J. Mol. Catal. A 361–362 (2012) 29–35.

[50] Q. Yuan, L. Chen, M. Xiong, J. He, S.L. Luo, C.T. Au, S.F. Yin, Chem. Eng. J. 255 (2014) 394–402.

[51] Y. Xu, M.A.A. Schoonen, Am. Mineral. 85 (2000) 543–556.

[52] G. Liu, P. Niu, L.C. Yin, H.M. Cheng, J. Am. Chem. Soc. 134 (2012) 9070–9073.

[53] W.J. Wang, J.C. Yu, D.H. Xia, P.K. Wong, Y.C. Li, Environ. Sci. Technol. 47 (2013) 8724–8732.

[54] S.H. Liu, X.D. Sun, J.G. Li, X.D. Li, Z.M. Xiu, H. Yang, X.X. Xue, Langmuir 26 (2010) 4546–4553.

[55] M. Nishikawa, Y. Mitani, Y. Nosaka, J. Phys. Chem. C 116 (2012) 14900–14907.

[56] W.J. Wang, L.Z. Zhang, T.C. An, G.Y. Li, H.Y.Y. Yip, P.K. Wong, Appl. Catal. B 108–109 (2011) 108–116.

[57] W.Q. Cui, W.J. An, L. Liu, J.S. Hu, Y.H. Liang, Appl. Surf. Sci. 319 (2014) 298–305.